LAWRENCE
LIVERMORE
NATIONAL
LABORATORY

LLNL-SR-645792

Simulation of Wind Turbine Performance and Loading Patterns using a Coupled Meso-scale/Micro-scale Flow Analysis Model

J. Sitaraman

November 7, 2013

Disclaimer

This work performed under the auspices of the U.S. Department of Energy by Lawrence Livermore National Laboratory under Contract DE-AC52-07NA27344.

Simulation of Wind Turbine Performance and Loading Patterns using a Coupled Meso-scale/Micro-scale Flow Analysis Model

Grant Number : B602825
Final Report
Period of performance : 12/13/2012 to 9/30/2013

Jay Sitaraman
Assistant Professor
University of Wyoming

Table of Contents

1. Summary

Task Statement	Progress
A1: Validation of performance and wind deficit characteristics of the WPS-30 turbine from the Sexbierum wind site using Helios/WRF meso-scale/microscale analysis model. Extension of the solution process to an actual wind farm	Performance and wind deficit characteristics of WPS-30 turbine have been compared using coupled HELIOS/ WRF solution framework. Results were presented at the AIAA Wind energy symposium in January 2013 and the forum of AHS in May 2013. In addition three articles have been submitted (two to Wind Energy Jounal and one Journal of Wind Engineering and Industrial Aerodynamics) towards archival publication (Details in Section 2.1)
A2: Develop dynamic model of the Mitsubishi 1MW turbine (sponsor will provide additional geometric details) and force it using WRF generated atmospheric inflow specific to a given site (sponsor will provide details of the site)	The windpact 1.5 MW turbine was chosen as the approximate model for the Mitsubishi turbine because of lack of actual geometry data. Computations have been conducted for a representative inflow condition at the rated conditions. Detailed input of representative wind conditions are expected from collaborators at University of Oklahoma. (Details in Section 2.2)
A3: Construct synthetic ABL inflow conditions with different turbulent intensities,scales, shear distributions and stability conditions and characterize their effects on the power and loading pattern of the wind turbine	Synthetic inflow model using the Mann model has been implemented and tested in in-house flow solver FLOWYO, Helios and also in LLNL code (CGINS). Use of synthetic inflow in combination with WRF data has also been investigated. See (Details in Section 2.3)
D1 : Implement, test and validate actuator disk/line models in the Cg-WIND code	Both actuator disk and actuator line models are implemented in a fully parallel fashion in CGINS code. (Details in Section 2.4)
D2: Formulate, implement, test and validate meso-scale/microscale coupling capability in the CgWIND code	Algorithms have been implmented in CGINS for including both Mann Inflow and meso scale inflow from WRF as inflow conditions. Tests have been performed in both turbine free conditions and also in conditions where a single turbine operates in the actuator line mode (Details in Section 2.5)

2. Technical Section

2.1 Helios : power results and wake visualizations for single turbine

HELIOS simulations were conducted for the WPS-30 turbine from the Sexbierum experimental site. The MMCI module was used to include the effects of the atmospheric boundary layer using the strategy described in the methodology section. In Figure 1 , the thrust and power variation for the WRF/Helios (Meso-scale/micro-scale simulation) is compared with measured power and stand-alone Helios computations (uniform inflow). The unsteady variations in power and thrust caused by the turbulent inflow conditions is clearly evident from these figures. Note that the mean hub height velocity could not be exactly matched to the uniform inflow values of 8 m/s because of constraints in adjusting the geostrophic wind and roughness length in Meso-scale WRF simulations. The offset in mean power and thrust notable in the figures are because of the small difference in the mean wind speed. Nonetheless, these results provide proof-of-concept of the integrated Meso-scale/Micro-scale simulation capability developed as part of this work. To further substantiate the effects of turbulent inflow, flow visualizations (iso-surfaces of vorticity overlaid on contours of velocity magnitude) are shown in Figure 2 . Meandering of the vortex wake and eventual breakdown are observed in the flow visualizations. Vortex breakdown is observed to occur between 1.5 and 2.5 diameter distance from the turbine. In uniform inflow (not shown here), the vortex wake persists to much longer distance of about 5 diameters before beginning to breakdown. It is expected that the vortex breakdown will be strongly correlated with the turbulence intensity of the inflow. The capability developed herein provides enabling technology for analyzing and characterizing such effects.

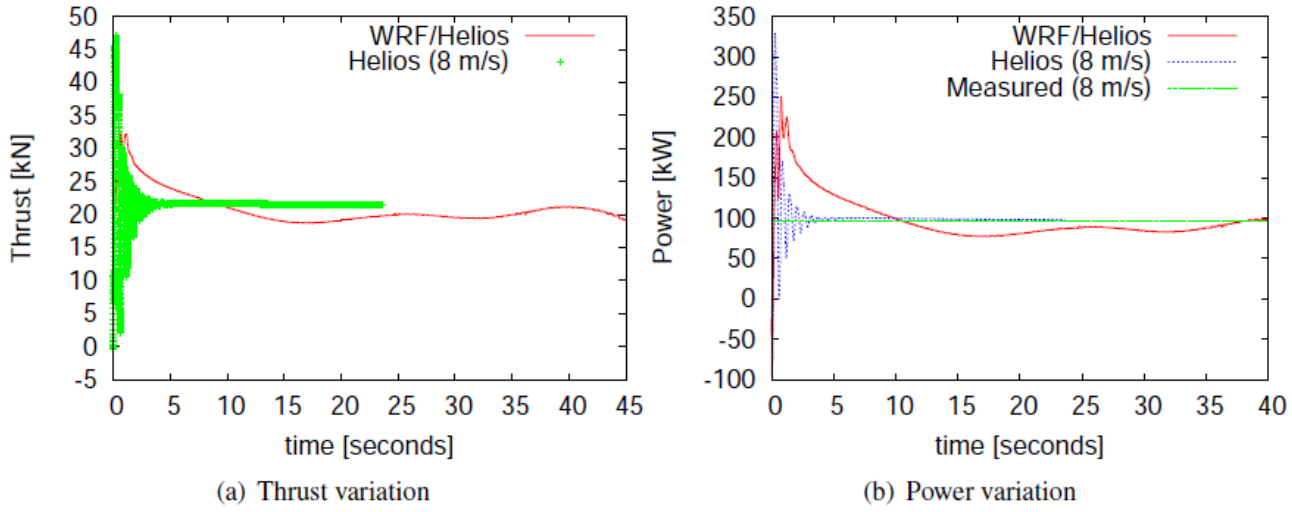

(a) Thrust variation (b) Power variation

Figure 1: Thrust and power variation obtained from coupled WRF/Helios simulations compared with stand alone Helios computations

Full simulation of the Lillgrund wind farm (48 turbines) were also performed using Helios. It is worth noting that this is the first wind farm simulation to be ever performed using full geometric model for the rotors and tower. Note that this case is simulated using uniform inflow. Computations using turbulent inflow conditions obtained from Meso-scale simulations are in progress.

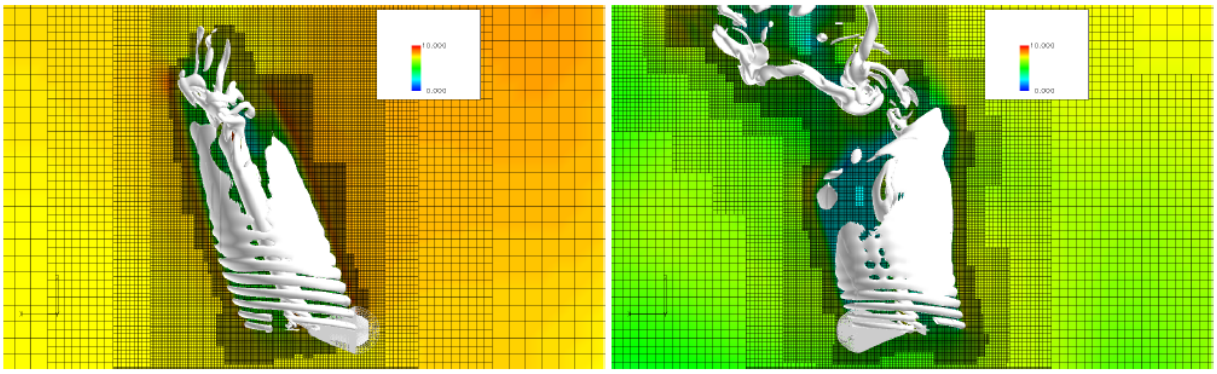

(a) t=11 seconds (b) t=59 seconds

Figure 2: Iso surfaces of vorticity (w= 0.003) overlaid with velocity contours. Grid systems are also overlaid on the flow visualizations to show the efficacy of solution based AMR.

Figures 3 and 4 show the velocity contours overlaid with vorticity magnitude contours in the hub-plane of the turbines and a vertical plane through a row of turbines respectively. It is evident that the vortex wake from each turbine is preserved with low dissipation rate until it interferes with the following turbine. This interference causes loss of power for the rear turbines. Power variation in two representative rows (4 and 7) are shown in Fig 5. Two trends are evident in the power variation plots. They are (a) the first rear turbine in a row shows the maximum power loss and the subsequent turbines maintain the same power level as the second turbine (b) When a turbine is missing (in row 4), the subsequent turbine shows a large recovery in power. Even in uniform inflow conditions, turbine-turbine interaction introduces increased wake dissipation and meandering. This is the reason for the trend noted in (a), because of increased turbulent dissipation the wake shadow effect caused the later turbines in each row are decreased.

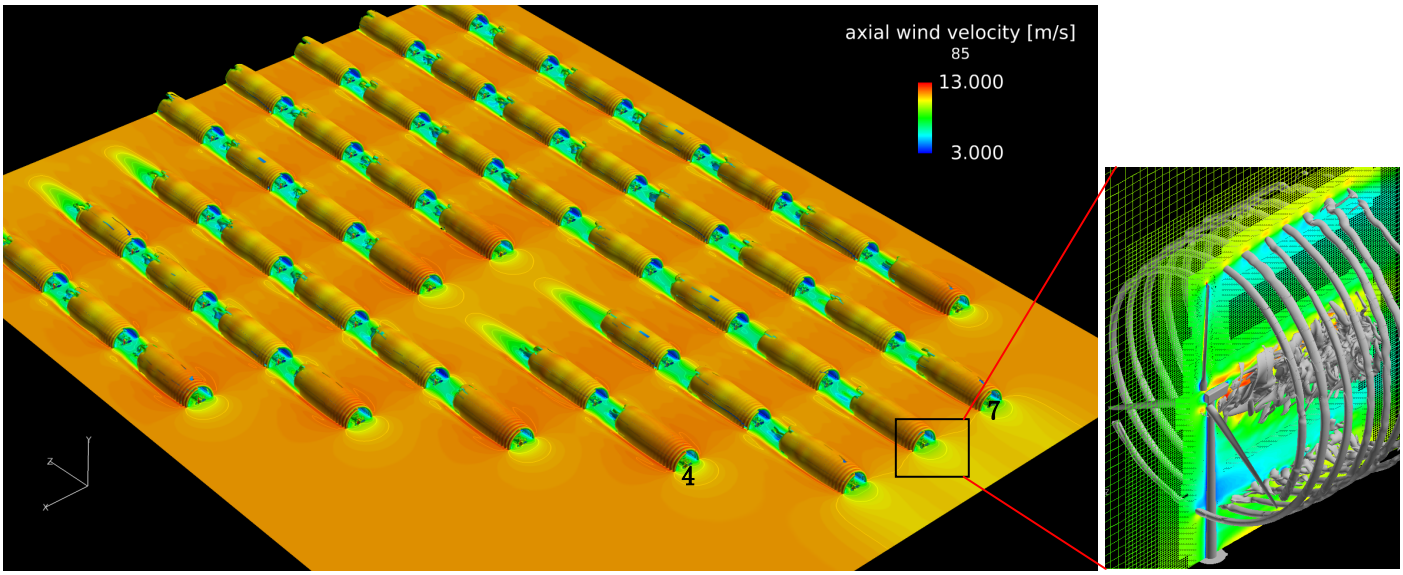

Figure 3: Vorticity contours overlaid with velocity field contours on the rotor hub plane for the Lillgrund wind farm. Inset adaptive mesh refinement shown in the vicinity of the leading turbine

The data presented is representative of a very low turbulence wind condition where flow can be

considered uniform. In more realistic scenarios, turbulent inflow will cause additional dissipation of the vortex wake and hence mitigate the amount of power deficit seen in following turbines in each row.

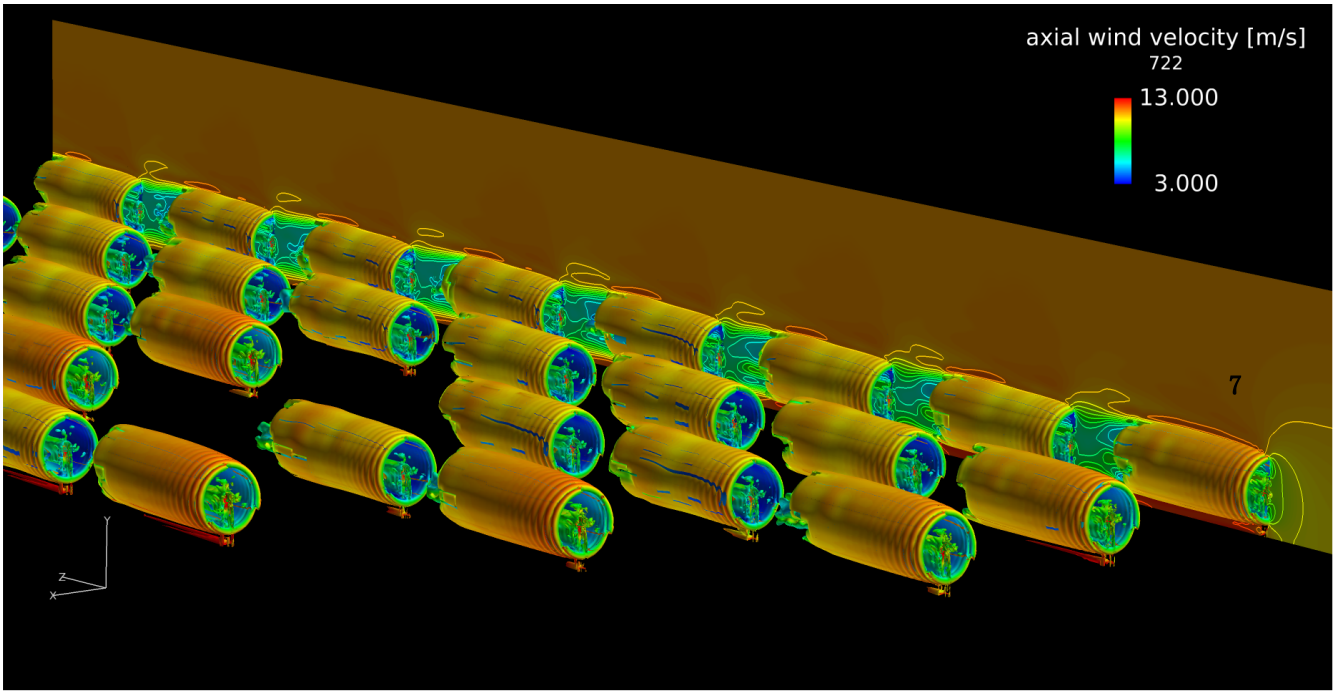

Figure 4: Vorticity contours overlaid with velocity field contours on a vertical plane that passes through row B

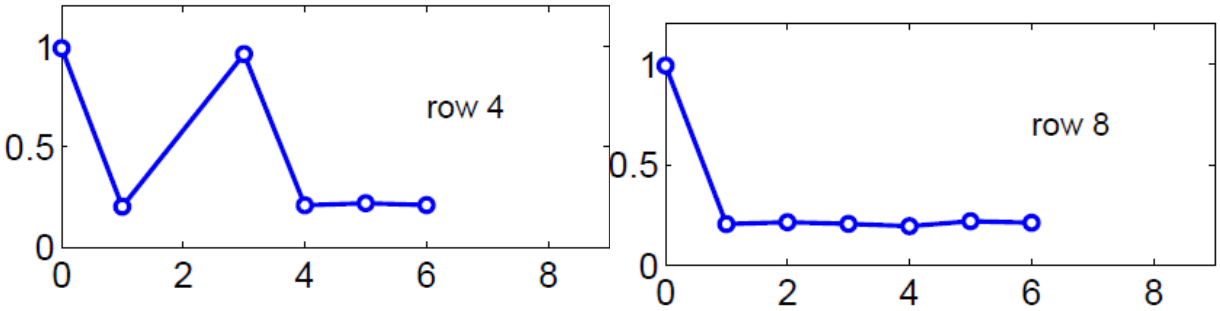

Figure 5: Power variation along rows 4 and 8 of the Lillgrund wind farm (x-axis is the rank of the turbine in that row and y-axis is power non-dimensionalized by the power of the leading turbine)

2.2 Sexbierum Wind Farm : HELIOS results and comparisons with other methods and available data

The Sexbierum wind farm is an experimental Dutch wind farm located at approximately 4 km from the seashore in the northern part of The Netherlands. The wind farm location was chosen since the terrain is flat and is mainly filled with grassland. The wind farm has a total of 18 wind turbines with a total installed capacity of 5.4 MW. The turbines are arranged in a rectangular fashion with the spacing between the turbines being five and 8 rotor diameters along the horizontal and vertical lines, respectively. The direction of the rows is at 7o with the north. Detailed measurements were performed in the farm and is available for comparison[1]. WRF simulations were performed using similar setup as for the single turbine case discussed before. The only difference was the change in the roughness

length. This value was changed from z0 = 0.1 m to z0 = 0.047 m to adjust it for the terrain at the Sexbierum wind site. The data from the WRF simulations were collected for 5 minutes with a sampling time of 1 second. Figure. 6 shows the profile of the mean wind speed and the turbulent intensity averaged over the 5 minutes interval. The hub-height is located at zhub = 35 m. At the hub-height, the wind speed and turbulent intensity was found to be 8 m/s and 12%, respectively. These values are close to the existing conditions at the wind farm. The CFD simulations were performed using all the three CFD solvers for the turbulent inflow cases. Figures. 7a-c

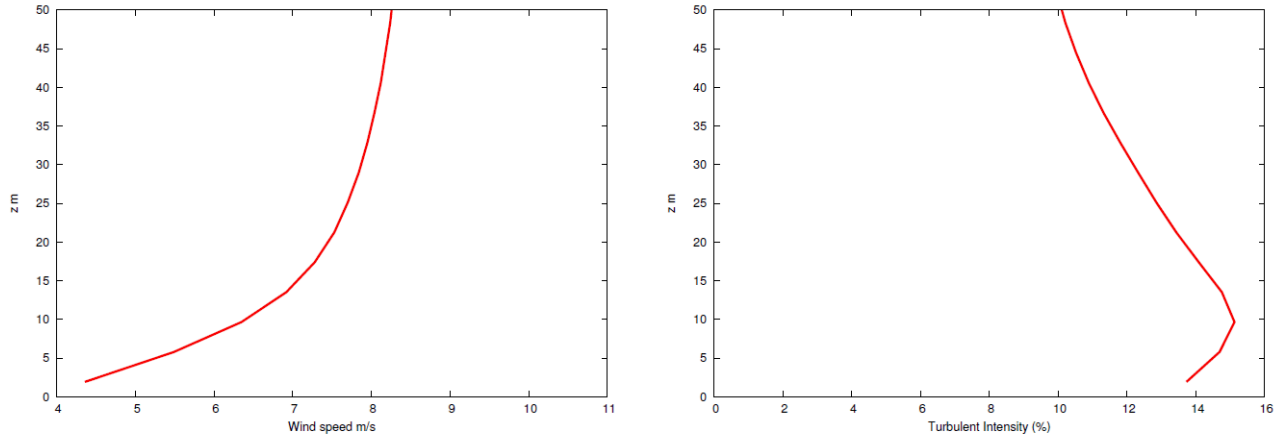

Figure 6: Mean wind speed and turbulent intensity from the precursor WRF simulations for the Sexbierum wind farm: (a) Wind speed and (b) Turbulent Intensity.

show the comparison of the wind speed, shear stress and TKE at the hub-height, predicted by the CFD solvers for a single turbine in the first row. The grids for the simulations were designed according to the conditions discussed before. Flowyo simulations were performed using both the actuator disc and actuator line models for the wind turbine. HELIOS simulations did not have a wall-function at the lower boundary and used symmetry instead. We do not expect that this will significantly affect the results at the hub-height. The results were compared with measured data at the wind farm site [1]. As expected, all the solvers show a maximum velocity deficit when the wind direction is aligned along the turbine axis. As, the wind direction changes, it results in partial wake situations and there is a decrease in the wake velocity deficit. The results obtained from HELIOS shows the best agreement with the measured data due to the modeling of the actual wind turbine and turbine wake. However, the interesting result that we see is the better comparison of the free vortex code with the experimental data compared to the Flowyo simulations. The results obtained using Flowyo can be potentially improved further by using a more refined grid for the simulations. However, this raises a question about the advantages of using a LES CFD code with a wind turbine model rather than a free vortex wake method. To better answer this question and provide a reason for using CFD codes, let us take a look at the turbulent shear stress and TKE as a function of wind speed direction. The accurate prediction of these parameters are essential to correctly predict the turbine loading and also understand the effect of the wind farm on the atmosphere. The shear stress data from experiments were not available and the results are compared with HELIOS for comparison. The comparison of the stresses are shown in Fig. 5b between the different solvers. Unlike the wind speed, there are significant differences in the profile of the shear stress between HELIOS and the other CFD solvers. Similar to the wind speed, the profiles of shear stress obtained from Flowyo can be improved using grid refinement. However, the UWake predictions cannot be improved by the addition of more markers. There is currently no mechanism in the free vortex model to account for the turbulent diffusion of the wake. The effect of these differences

in the shear stress predictions are further demonstrated from the plot of TKE in Fig. 5c. When the wind direction is along the turbine axis, the free vortex code gives a good prediction of the TKE. However, when the wind direction is outside the range of [-20,20] degrees, the TKE is significantly over predicted by UWake while all the other methods provide good agreement with measurements. A new free vortex model with additional terms to account for the turbulent diffusion is being investigated in a complementary paper to resolve this issue. We expect that this new model should be able to improve the predictions obtained from UWake.

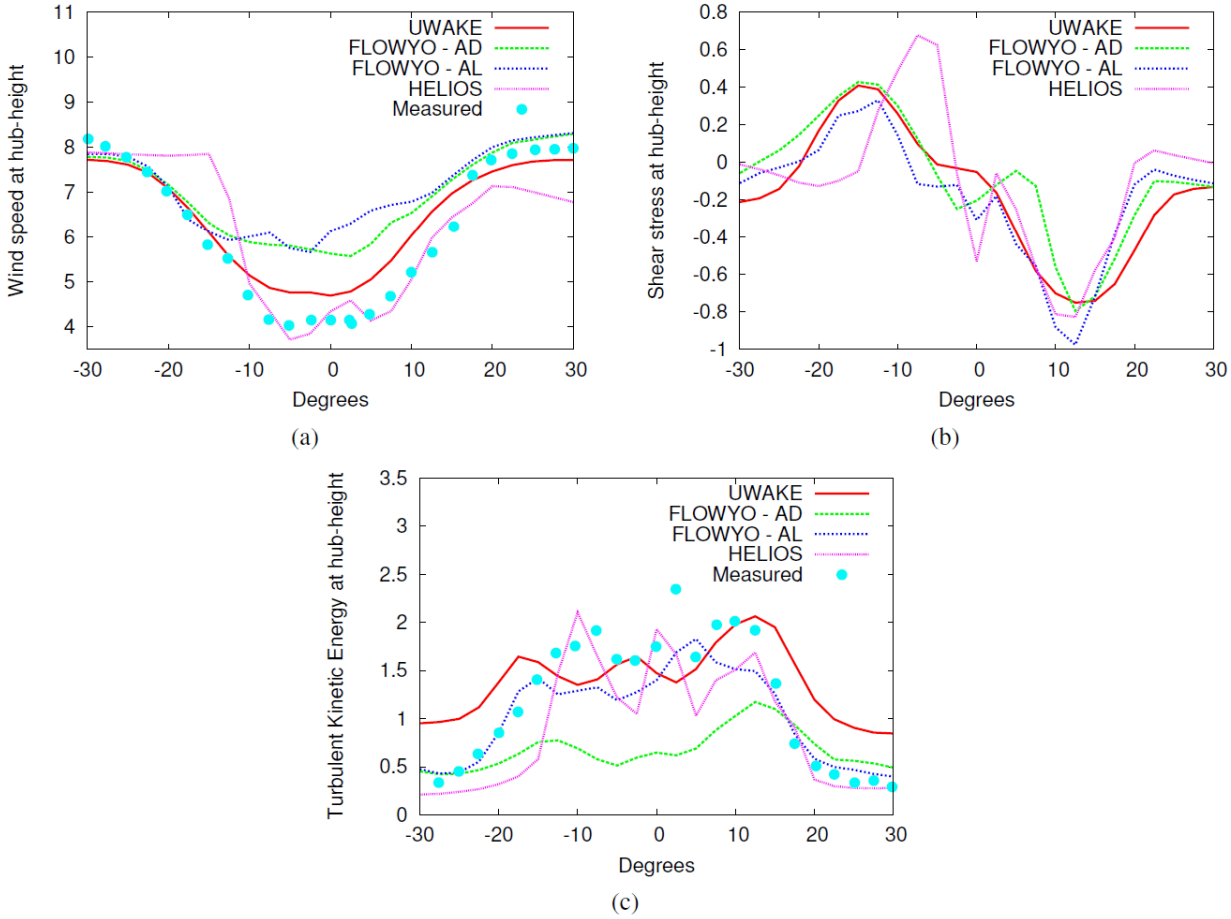

Figure 7: Comparison between the different CFD solvers at 2.5D downstream of a single turbine in the first row:(a) Mean wind speed as a function of wind direction and (b) Mean shear stress as a function of wind direction.

2.3 Preliminary analysis of the WINDPACT turbine (surrogate for the Mitsubhishi 1.5 MW turbine)

The geometry data for the WINDPACT turbine was obtained from the technical reports available at (http://www.nrel.gov/wind/windpact.html). The turbine is composed of S818/S825/S826 section with a 10 degree linear twist and 3:1 taper ratio. The maximum chord length of 0.08R occurs at radial locations of 0.25R. The root region of circular section of diameter 0.05R upto a radial location of 0.07R, which then transitions to an S818 airfoil section at 0.25R radial location. Figure 6 shows the mesh surface was generated by laying the airfoil sections according to their taper and twist. A structured mesh shown in Figure 7 was generated using an in-house grid generator and was utilized for

obtaining flow solution using Helios.

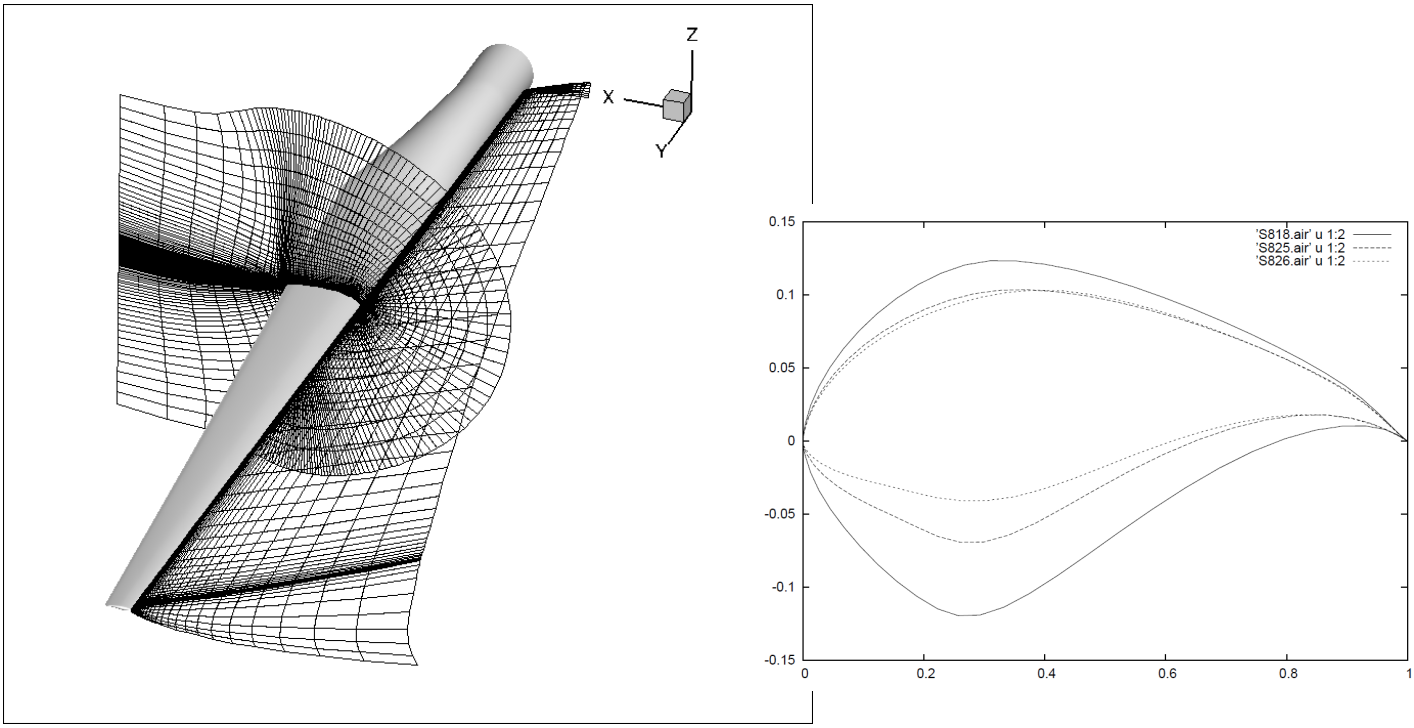

Figure 6: Blade surface and airfoil shapes used for the WINDPACT 1.5 MW turbine. Two representative planes of the structured volume grid generated is also shown

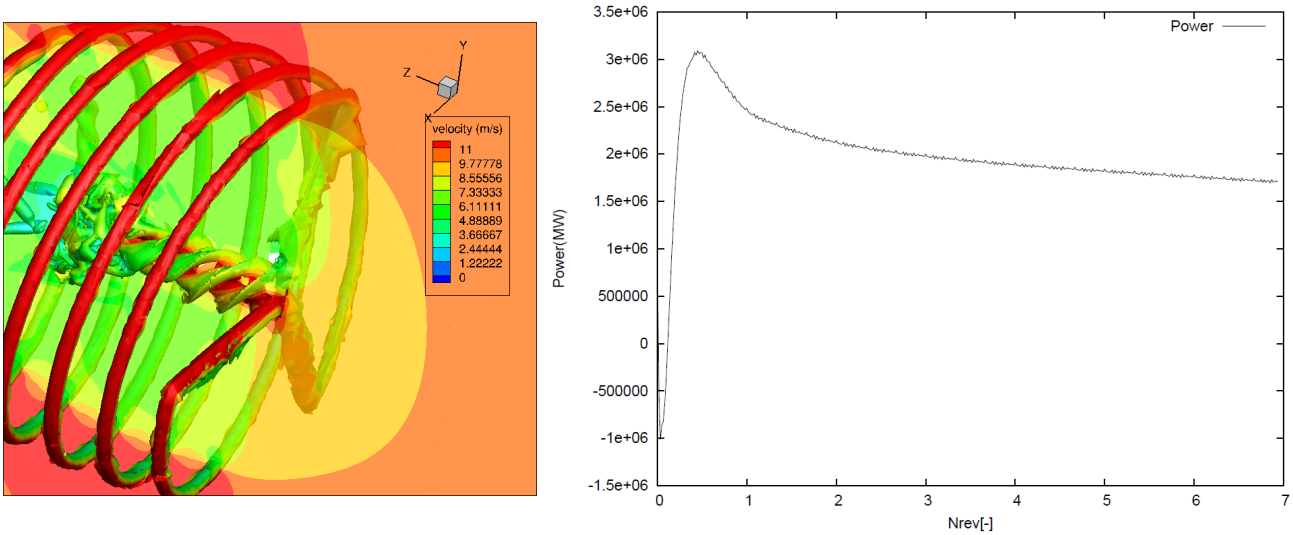

(a) Vorticity iso-surfaces overlaid with velocity contours

(b) Power variation with number of rotor revolutions

Figure 7: Preliminary solution for the 1.5 MW WINDPACT turbine geometry at uniform inflow conditions.

2.4 Implementation of Synthetic Inflow

Motivation:

Figure. 8 shows the comparison of the wind speed at hub-height (z = 65 m) for a single turbine blade used at the off-shore Lillgrund wind farm [2]. Both these simulations have been performed using with an actuator line parametrization of the turbine blade. The grid resolution for these simulations were 8min the streamwise and spanwise directions and 4 m in the vertical direction and the tip-speed ratio was around $\lambda = 8$. The average power predicted from both these simulations are comparable to each other suggesting that the average power is not significantly affected by atmospheric turbulence. However, there are differences that can be observed in the wake structures which can influence the power produced by the turbine operating in the wake of this turbine. Our previous studies have shown that these differences can be significant for an entire wind farm and can change the total amount of power produced by the turbines operating in uniform or turbulent inflow. Although, these results are encouraging regarding the capability of the coupled mesoscale-microscale solver, there are a number of issues which have to be addressed. These are:

1. Breakdown of vortex structures: Previous studies by Troldborg et al. [3] have shown that for a single turbine operating in uniform inflow at $\lambda = 8$, the wake behind the turbine eventually breakdowns at approximately 10 diameters downstream. The breakdown location moves further upstream with increase in the tip-speed ratio. However, this was not observed in our simulations even at tip-speed ratios of 12. For the turbulent inflow case, the wake breakdown occurs at less than 2 diameters downstream at the tip-speed ratio of 8. However, this is not the case either and the turbulent structures are not visible at the hub-height and seems to have been dissipated.

2. Flow structures and wind turbine response: Figure. 8 (a) and (b) show the comparison of the velocity field at z = 65 m for two different WRF simulations of neutral boundary layer using a domain size of 2048x2048 x 1024 m and grid resolutions of 128×128×256 and 512×512×512, respectively. The comparison of the energy spectrum for both these cases are shown in Fig. 8(c). It can be clearly seen that there are significant differences between the energy content beyond wave number of $\kappa = 0.1$.

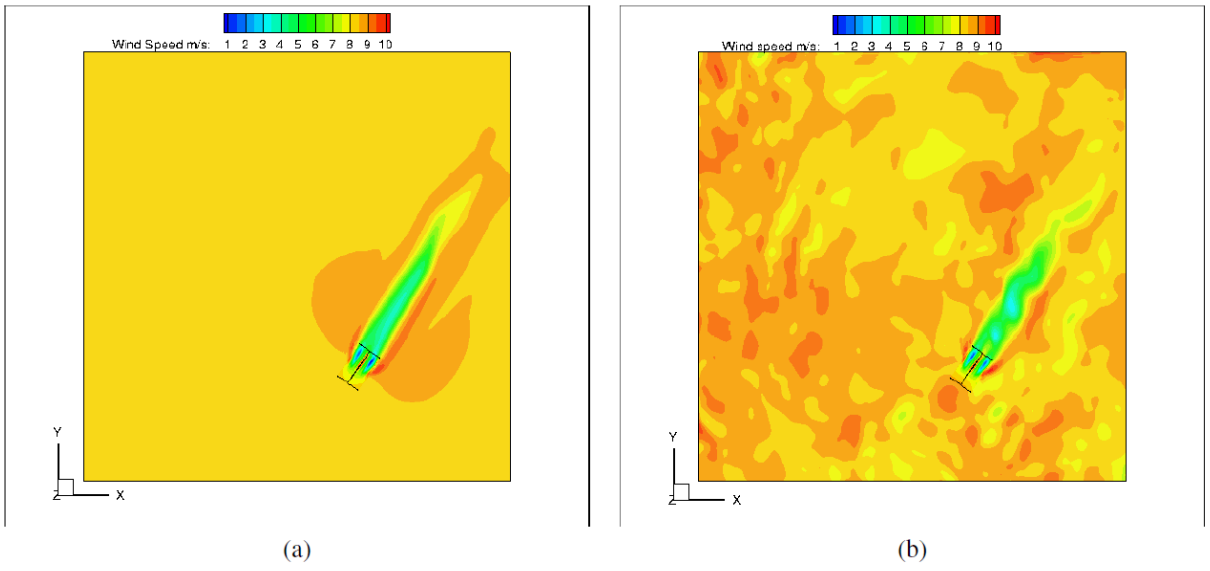

Figure 7: Instantaneous wind speed at hub height for single turbine blade used in the off-shore Lillgrund wind farm: (a) Uniform inflow and (b) Turbulent inflow obtained from WRF simulations

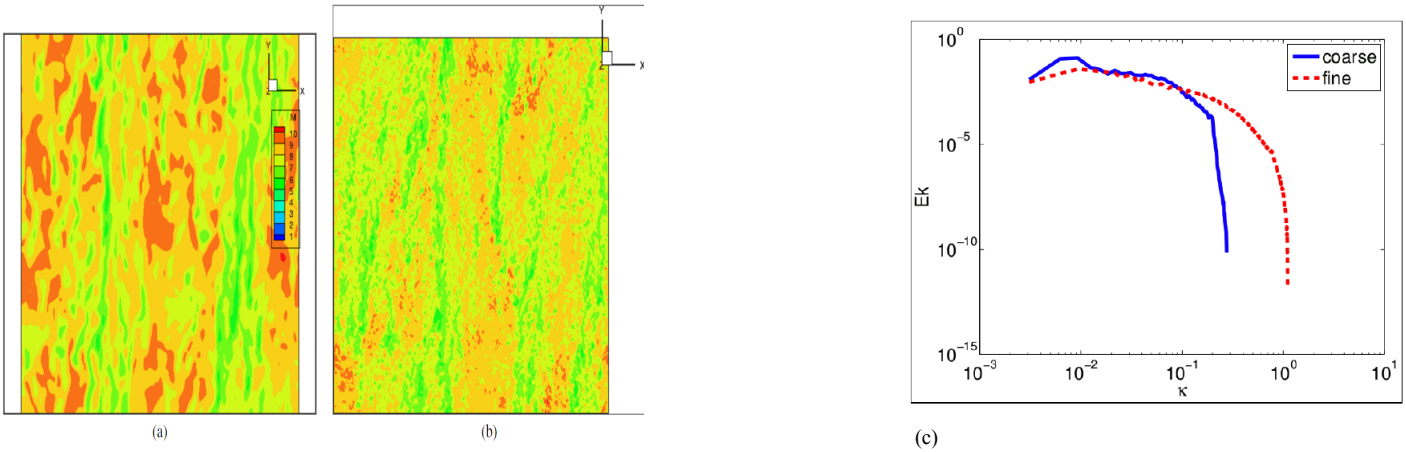

Figure 8: Comparison of the wind speed at z = 65mfor a neutral boundary layer on a domain size of 2048x2048x1024m obtained from WRF: (a) Grid resolution of 128 × 128 × 256 and (b) Grid resolution of 512 × 512 × 512 (c) Comparison of the energy spectrum at z = 65 m for the coarse and fine grid cases in the previous (a) and (b).

Synthetic Inflow implementation:

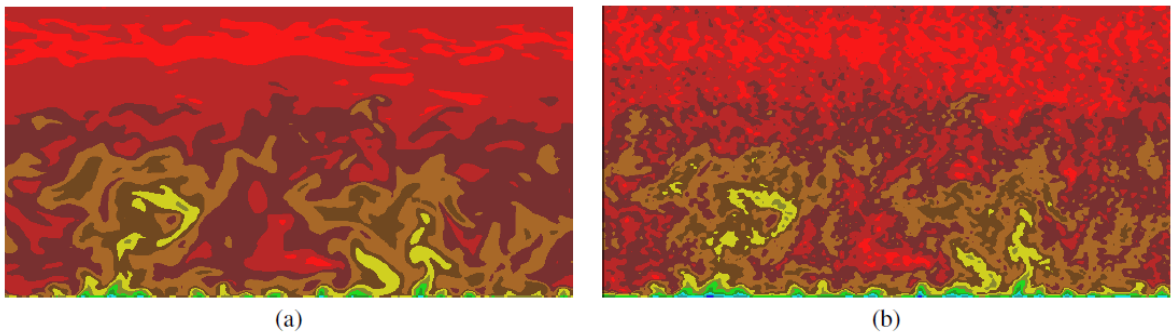

Figure 9: Instantaneous wind speed along a spanwise plane to demonstrate the synthetic small-scale model: (a) No added fluctuations and (b) Fluctuations added using the small-scale model.

The analysis in the previous section revealed the importance of resolving the flow structures up to dx = 1 m for studying the dynamic response of the wind turbine. However, computations at such small grid resolutions are not possible for the atmospheric boundary layer. Hence, as an alternative for using realistic inflow conditions, synthetic inflow generators have often been used to provide inflow conditions at very fine grid resolutions. These simulations are tractable as the size of the domain size becomes one-tenth of the ABL domain size with synthetic inflow. However, studies of stable boundary layer by Park et al. [6] have revealed that the turbine-scale variables like wind-speed, wind shear, etc. are strongly inter-related and should not be prescribed independently. Most of the synthetic inflow generators do not currently have the capability to account for the relation between the different variables and the difference in results due to independently prescribing them is unclear. To understand this issue and provide a viable solution, a synthetic inflow generator module based on the algorithm developed by Mann [7] has been added to the mesoscale-microscale coupling interface (MMCI). This algorithm is based on a model of the spectral tensor and is capable of simulating all three components of a three-dimensional incompressible turbulence field. Furthermore, it can simulate turbulence with the same second order statistics as the atmosphere. The details of the model can be found in Refs. [3, 7]. The model allows the generation of anisotropic fluctuations and the ability to specify the turbulent intensity. However, the model is applicable only to neutral boundary layer. Hence, the synthetic inflow has been implemented in two different forms:

1. Inflow model: In this form, the flow-field is decomposed as follows

$$u_i(\vec{x},t) = U_i(\vec{x}) + u_i^{'}(\vec{x},t)$$

where u_i is the inflow velocity, U_i is the mean inflow velocity and u'_i is the fluctuations generated by the model. U_i can be specified using a log-law or power law. This form is applicable only for the neutral boundary layer.

2. Small-scale model: In this method, the flow-field is decomposed as follows

$$u_i(\vec{x},t) = U_i(\vec{x},t) + u_i^{'}(\vec{x},t)$$

where $U_i(x, t)$ is the inflow velocity condition from LES of the atmospheric boundary layer and $u'_i(x,t)$ is the resolvable fluctuations which are generated using Mann model. To understand the meaning of this term, let us consider Fig.7(b). The turbulent inflow was generated using a horizontal resolution of 16 m while the FLOWYO simulations are performed using a horizontal resolution of 8 m. Hence, there is a portion of the energy spectrum between dx = 16 m and dx = 8 m which can be resolved in the FLOWYO simulations but are not resolvable in the ABL simulations performed using WRF. The resolvable fluctuations refers to the added fluctuations to account for this missing part of the spectrum. This is accomplished by modifying the spectrum that is provided as input to the Mann model as follows

$$E(k) = E(k)\frac{k^4}{k_0^5}\exp\left(-2\left\{\frac{k^2}{k_0^2}\right\}^2\right)$$

where k_0 is a cut-off frequency that has to be specified. Presently, this parameter is specified as $k_0 = 0.9\ k_u + 0.1\ k_l$ where k_l is the highest resolvable wave number in the ABL grid and k_u is the highest resolvable wavenumber in the FLOWYO grid. Trial and error is required to accurately specify this parameter. This model can be theoretically used for convective and stable boundary layers. However, simulations have to be performed to investigate any deficiencies.

The ability of the small-scale model to add fluctuations over a specified range of wavenumbers is shown in Fig. 9. Figures 9a and b show the wind speed before and after the addition of fluctuations for a FLOWYO horizontal resolution of 8 m with a WRF inflow resolution of 16 m. It can be seen that the fluctuations have been added only at the smaller scales. To show that the method works, the simulations using turbulent inflow have been repeated using the modified inflow conditions for the turbine blade used in the Lillgrund wind farm. The hub-height wind speed is shown in Fig. 10. It can be seen that the use of the modified low dissipation scheme with synthetic inflow generates and preserves turbulent structures which have been dissipated in the previous simulations. Presently simulations are being performed for the Lillgrund wind farm using the modified inflow approach and also to compare the performance of the synthetic inflow model with the synthetic small-scale model. This modified synthetic inflow model in MMCI works with UWake, FLOWYO and HELIOS without any additional modifications

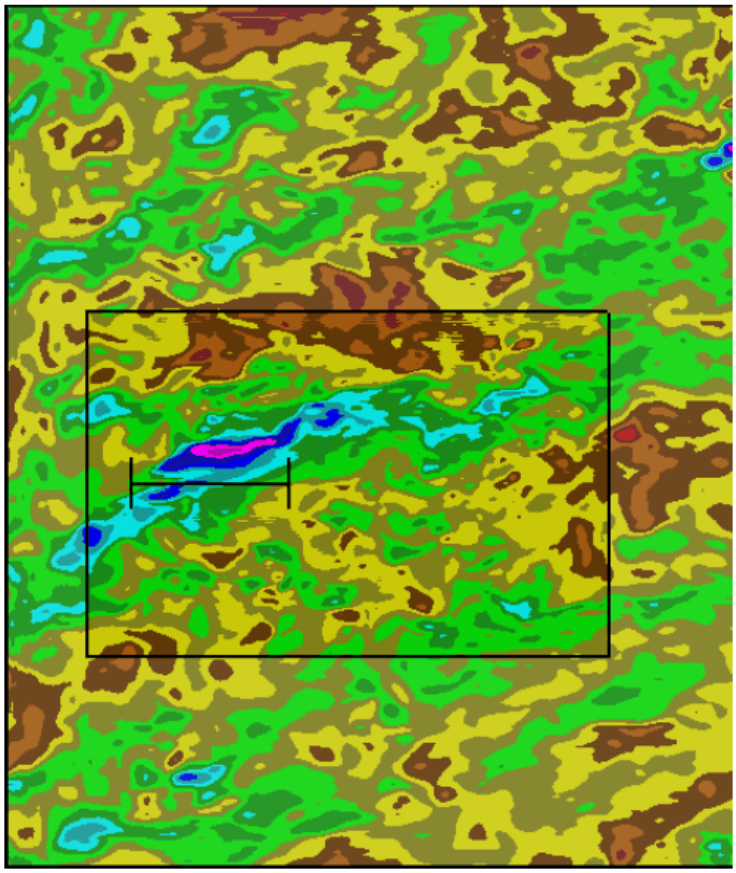

Figure 10: Wind speed at hub-height (z = 65 m) for turbine blade used in the Lillgrund wind farm. The inflow condition has been modified using the synthetic small-scale model.

2.5 Actuator Models in CGINS

Three different methods have been tested and implemented for performing actuator simulations of wind turbine in CGINS.

Momentum disk

In the first approach, one-dimensional momentum theory is used to calculate the body force from the actuator disk. The thrust force due to the turbine is calculated as follows

$$F_x = \frac{\rho_0 U_0^2}{2} A C_T$$

where U_0 is the undisturbed wind speed that the turbine sees, A is the face area and C_T is the thrust coefficient of the wind turbine, assumed constant for the entire domain. Although this is a very simplified representation of the wind turbine, this drag model has been successfully used to study spectral coherence in LES of turbine wakes. This model can be used directly used with or without the generation of overlapping grids in the near-body region of the turbine.

Sample result obtained using this approach for six hypothetical turbines arranged in a 2 × 3 array (radius 0.5 m and $C_T = 0.4$) is shown in Fig. 11 without overlapping grids. This method works in serial and parallel. This method was implemented for testing purposes to understand the inner workings of the CGINS code.

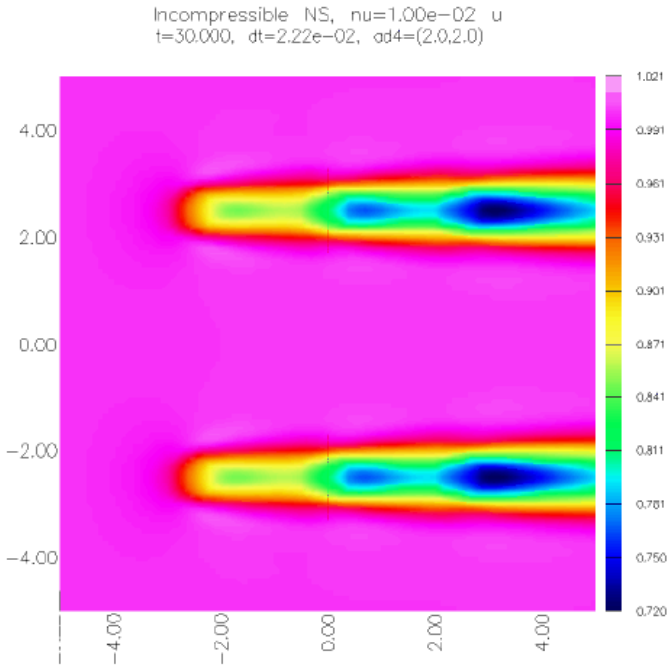

Figure 11: Wind speed at hub-height for a 2×3 wind turbine array obtained using a simplified drag model in CGINS.

Actuator Disk

In the second approach, the body force due to the wind turbine has been calculated in detail using the blade element theory. This body forcing has been implemented in CGINS by adding a Fortran module "actuatorForcing.f" as an extern C function. This function acts as the driver and calls the actuator disk routines and calculates the power, thrust and loading. Briefly, the actuator disk routines take inflow velocities computed by CGINS as input and provide the source terms for the momentum equations as output. The source terms are computed as a temporal average. The methodology is as follows:

1. At any time level, the velocity at all locations in the plane of the wind turbine rotor is known from the flow states. Here the wind turbine rotor is constrained to a grid plane of the cylindrical grid.

2. The actuator disk model utilizes blade element theory, whose basic mechanism is to compute sectional forces along a turbine blade using lift and drag values from an airfoil lookup table. Lift and drag depend on the angle of attack at each span station, which is in turn computed using the rotational speed of the turbine and the inflow velocities obtained from the flow solver.

3. Forces in all coordinate directions are now available at every azimuthal location of the blade. If there are N such locations (this is the azimuthal dimension of the cylindrical grid), the probability that the blade will be at that location is 1/N . Therefore the loading along each grid line is scaled by this factor and computed as a source term for the momentum equations. CGINS requires force/unit volume, therefore the point force computed is divided by the corresponding cell volume and this force is provided as the source term.

4. To summarize the mechanism of coupling is as follows: The flow solver computes flow states (momenta and pressure) – the blade element model computes the aerodynamic loading in response to these flow states – source terms that depend on this aerodynamic forcing is provided as a feedback

response to flow solvers. As iterations progress, both flow states and aerodynamic loading converge to a steady state.

This method has been setup to work with a cylindrical near-turbine grid overlapping a Cartesian off-body grid. The method currently works in serial mode and is compatible with parallel execution as well. Parallel execution has not been conducted for the actuator line because inherent difficulty that CGINS has with partitioning grids of cylindrical topology. Sample result for the NREL phase VI wind turbine using the actuator disk approach in CGINS is shown in Figure 12. The fourth-order dissipation coefficient have been set to higher values than required to provide numerical dissipation as an alternative to SGS model.
In Figure 13, the evolution of mean velocity at the rotor plane, power and thrust are shown for the NREL-phase VI turbine at V_{inf} = 10m/s. Results show expected trends, i.e. decrease in mean inflow velocity and progress of thrust and power towards steady state values. Since the simulations are serial, the computational time is prohibitive to march the simulation towards steady state. Parallel implementation and verification is intended next to fully validate the actuator disk implementation.

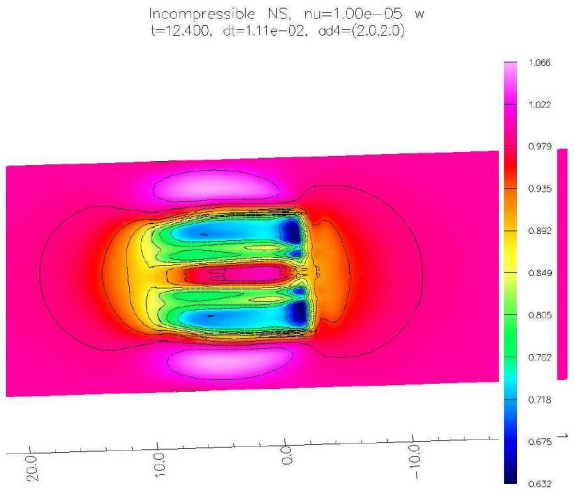

Figure 12: Demonstration of the actuator disk model in CGINS for NREL phase VI wind turbine.

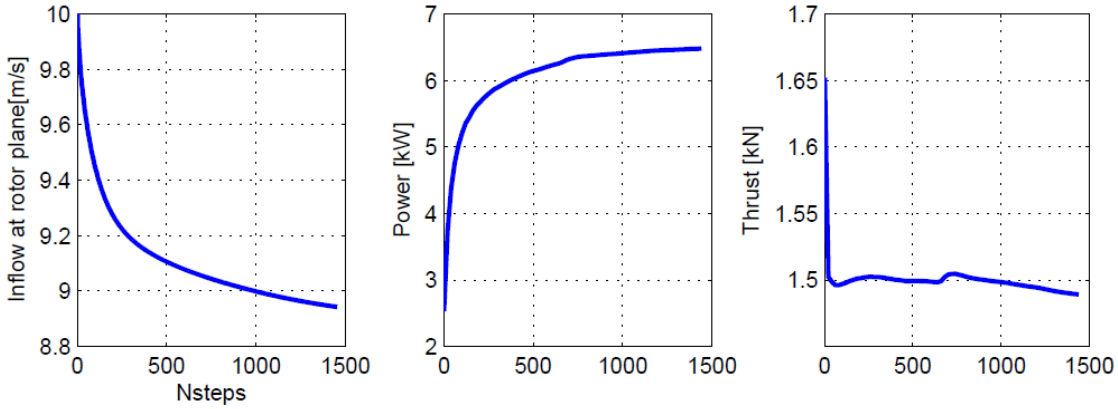

Figure 13: Evolution of (a) mean velocity at rotor plane (b) Power and (c) Thrust with time steps

Actuator Line

The actuator line approach is the most complex and versatile approach implemented in CGINS. Wind turbine blades and tower are represented as lifting lines (drag sources in case of the tower) in this method. In contrast to the actuator disk, the actuator line method produces discrete vortex sheets and structures from each of the rotor blades and tower. In addition, the implementation follows a 'grid agnostic' approach such that the actuator lines can be embedded in any grid system, Cartesian, Cylindrical or arbitrary curvilinear grids. In addition any number of turbines can be modeled simultaneously to create a large wind farm.

Briefly, the approach is as follows.

(1) Every blade and tower is represented as a line. If there are ***n*** turbines with ***b*** blades and 1 tower, there are in total n*(b+1) objects. Where each object represents a lifting line or drag source. All of these objects are distributed among processors in a parallel processing environment. The ideal scenario will be to have n*(b+1) processes, when the load will be equally distributed.

(2) Each object forms an inflated bounding box (inflated by one chord length) around its lifting line. At each time step each bounding box performs a search process (fully parallel) to create a point cloud of grid points from the mesh system around its lifting line (Shown in Figure 14 (a)).

(3) A least-square based interpolation technique is performed to interpolate the velocity field to the lifting line control points from the point cloud. Subsequently, Blade Element Theory based aerodynamic computations to evaluate forces at lifting line control points. Tabulated airfoil coefficient data is utilized to support these calculations.

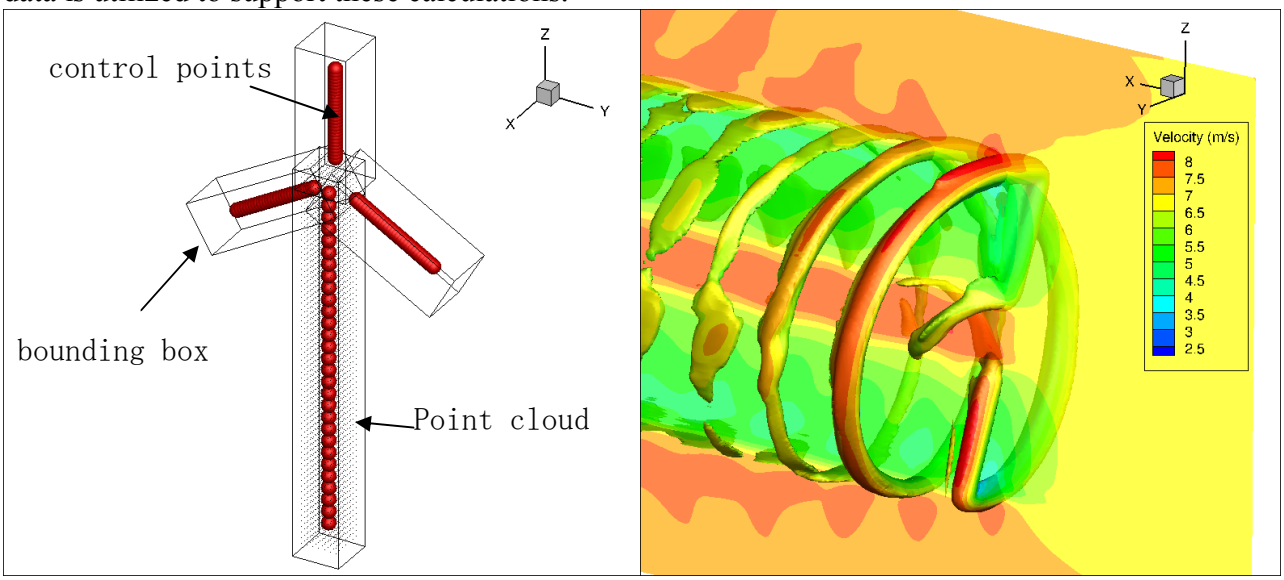

(a) (b)

Figure 14: (a) Actuator line parameterizations and (b) typical flow solution (vorticity iso-surfaces and velocity contours) for a two bladed turbine.

(4) The forces calculated at the lifting line control points are then distributed as source terms to the point cloud that encompasses it. A 3-D Gaussian convolution kernel is used to estimate individual contributions at each grid point that is included in the point cloud.

(5) Flow computations are performed using the native solver algorithms with the additional source terms. The lifting line systems are then moved according to their movement rules (e.g. rotor blades are rotated around their hub axis).

Steps 2 to 5 are repeated at each time step to perform a complete wind turbine simulation.
The actuator line model described above is implemented and tested in the CGINS framework. In Figure 17, validation for the NREL phase VI two bladed turbine is shown for yawed flow conditions at for different wind speeds and several yaw-angles. Fair comparison can be noted between experimental data and other models (Helios full rotor model and free vortex model).

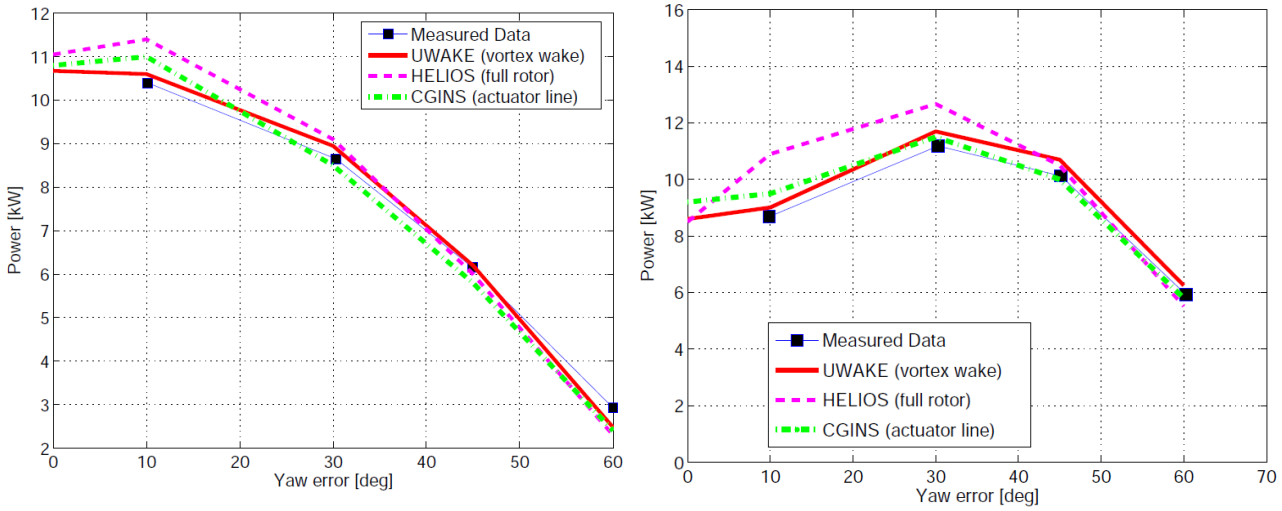

(a) V=10 m/s (b) V=15 m/s

Figure 15 : Comparison of actuator line model with full rotor and vortex wake models for yawed flow conditions of the NREL phaseVI two bladed rotor test case.

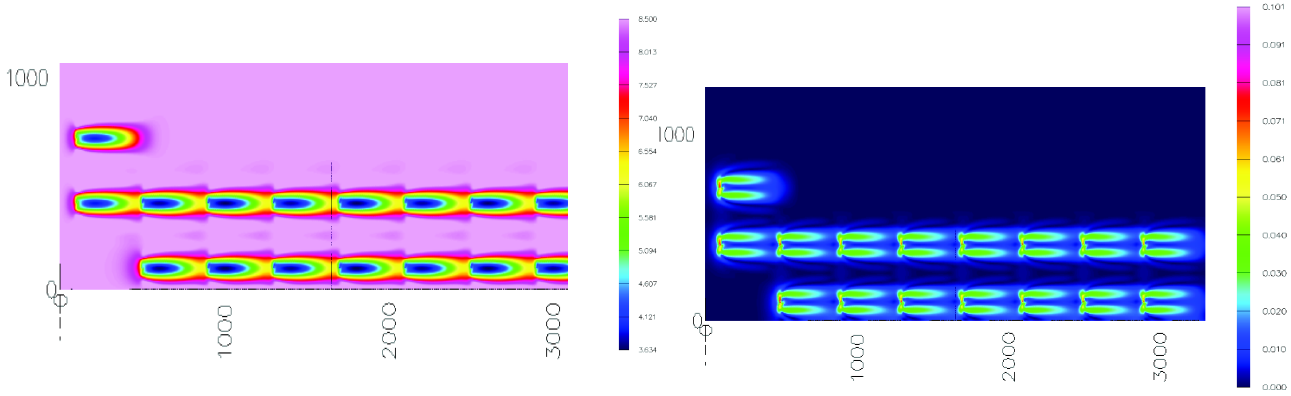

(a) Velocity contours (b) Eddy viscosity contours

Figure 18: Velocity and Eddy viscosity contours for a 16 turbine simulation in CGINS

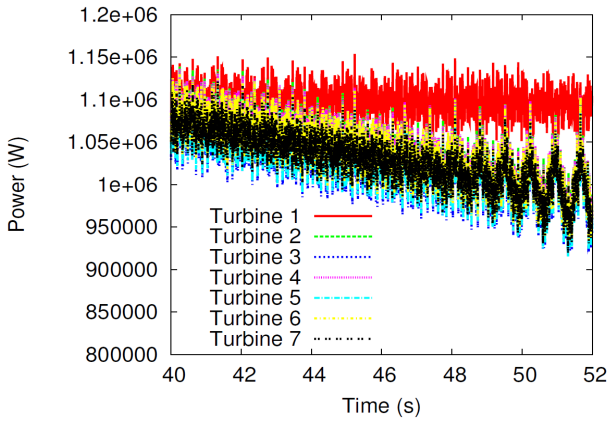

Figure 19: Power variation of turbines in the first row (bottom most from Figure 18)

Actuator line model was further tested for multi-turbine scenarios in a wind farm. A subset (with 16 out of the 48 turbines) of the Lillgrund wind farm is used as the initial test case. In Figure 18, the velocity and eddy viscosity contours are shown for the 16 turbine test case. Figure 19 shows the power variation of the turbines along the first row. Expected power for the leading turbine is about 1.2MW per specifications of the manufacturer. Since actual geometry is not known, a notional turbine with know airfoil characteristics was generated to match the actual turbine. Expected patterns of velocity deficits and increased turbulence behind each turbine is observed. These results provide further confidence to the implementation of the actuator line module. The 16 turbine computations were performed on 14 million point grid on 256 processors.

2.6 Meso-scale/Micro-scale coupling in CgWIND

The Meso-scale/Micro-scale coupling Interface (described in section 2.4) was extended to be used with CgINS as well. Appropriate velocity interpolation and eddy viscosity calculation procedures were implemented to make the execution seamless and consistent.

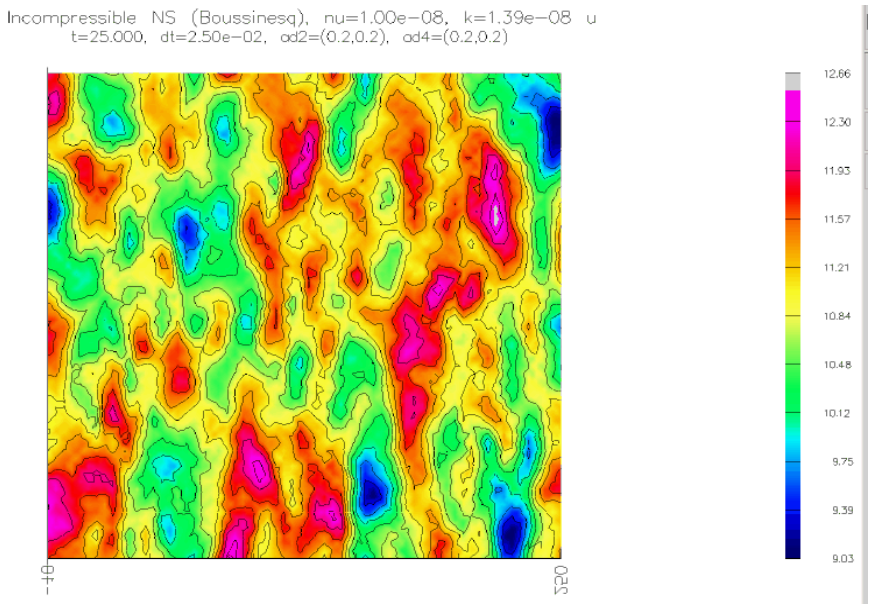

Figure 20: Turbulent inflow at the inflow plane of the CgINS grid system

In Figure 20, the axial velocity field (generated using synthetic turbulence data from the Mann model) is shown at a solution plane few characteristic lengths from the inflow plane. It can be noted that the prescribed turbulent inflow at the inflow plane is convected robustly and consistently by the solution algorithms in CgINS. Further, this figure provides proof-of-concept for consistent interpolation of the turbulent inflow conditions onto the inflow plane.

An 3-bladed wind turbine system was included to study the combined execution of Meso-scale/Micro-scale coupling and actuator line implementation. In Figure 21 the velocity and eddy viscosity field are shown for turbulent inflow conditions. Expected trends of faster wake breakdown and larger meandering of vortex wake is evident from these plots. Figure 22 shows velocity and eddy viscosity contours at an axial slice (x=30m) behind the turbine. The discrete nature of the vortex wake that is created by the actuator line model is evident in this figure. Increased dissipation of the velocity and eddy velocity fields caused by the presence of turbulent inflow can also be observed from Figure 22.

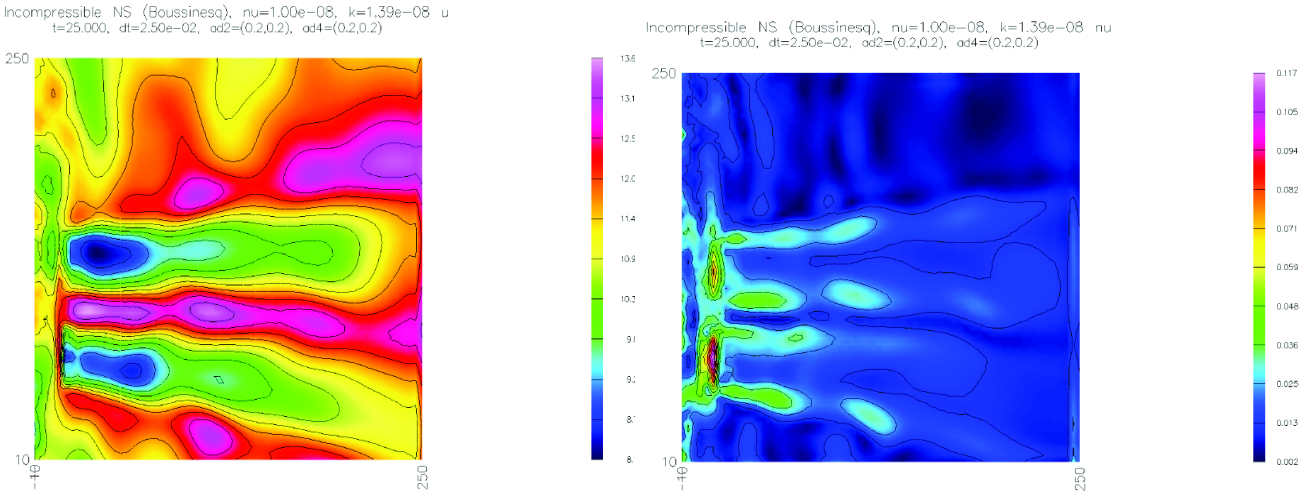

(a) (b)

Figure 22: Isolated turbine (Lillgrund, Vestas V80, R=43.5m) in turbulent inflow. U-velocity contours (a) and eddy viscosity contours (b) on a hub-plane slice (z=65 m)

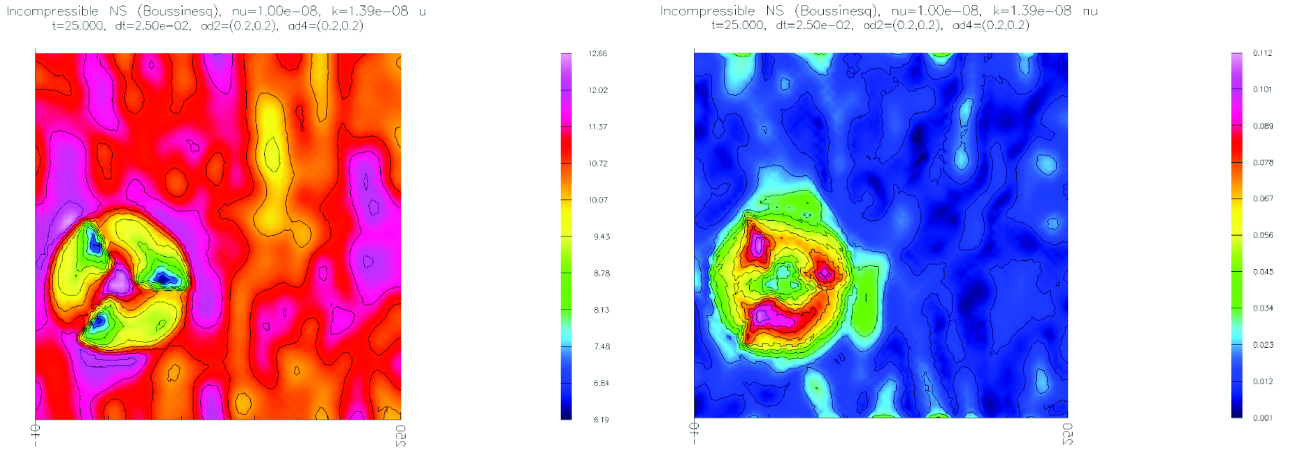

Figure 4: U-velocity (a) and Eddy viscosity (b) contours for isolated turbine in turbulent inflow at an axial slice (x=30) behind the turbine

3. Publications related to this work:

3.1 Conference Publications:

1. Sitaraman, J. , Mavriplis, D., Gopalan, H., Gundling, C, Roget, B., Brown, K., "Wind Farm Simulations on Massively Parallel Computer Systems Using Methods of Incremental Complexity," NAWEA 2013, August 6-9, Boulder, Co.

2. Sitaraman, J. , Gundling, C., Roget, B., Masarati, P. and Mavriplis, D., "Computational Study of Wind Turbine Performance and Loading Response to Turbulent Inow Conditions," Presented at the AHS 69th Annual Forum, Phoenix, Arizona, May 2123, 2013.

3. Gopalan, H., Sitaraman, J. and Heinz, S., "Simulation of Attached and Separated Flows using Realizable Linear and Non-Linear Hybrid RANS-LES Models", AIAA 2013-2949, 21st AIAA Computational Fluid Dynamics Conference, San Diego, CA.

4. Gundling, C., Gopalan, H., Sitaraman, J. and Roget, B., " A Free-vortex Wake Diffusion Model for Wind Turbines in Steady and Turbulent Atmospheric Inow," AIAA 2013-1207, 51st AIAA Aerospace Sciences Meeting including the New Horizons Forum and Aerospace Exposition, 2013, 10.2514/6.2013-1207

5. Sitaraman, J. , Gopalan, H., Gundling, C., Mirocha, J. and Miller, W., "Coupled Meso-scale/Microscale Model For Wind Resource Estimation and Turbine Aerodynamics Using and Overset Approach," 51st AIAA Aerospace Sciences Meeting including the New Horizons Forum and Aerospace Exposition, 2013, 10.2514/6.2013-1209.

3.2 Archival publications submitted

6. Gundling, C., Roget, B., Sitaraman, J. and Masarati, P., \Application and Validation of Incrementally Complex Methods For Wind Turbine Aerodynamics, Part 1: Isolated Wind Turbine in Steady Inow Conditions", Submitted to Wind Energy

7. Gundling, C., Gopalan, H., Roget, B., Sitaraman, J. , Mirocha, J. and Miller, W., \Appli-cation and Validation of Incrementally Complex Methods For Wind Turbine Aerodynamics, Part 2: Isolated Wind Turbine in Turbulent Inow Conditions", Submitted to Wind Energy

8. Gopalan, H., Gundling, C., Brown, K., Roget, B., Sitaraman, J. , Mirocha, J. D. and Miller, W.,A., "A Coupled Mesoscale-Microscale Framework for Wind Resource Estimation and Farm Aerodynamics", Submitted to Journal of Wind Engineering and Industrial Aerodynamics